Article

Helium reservoirs in iron nanoparticles on the lunar surface

Check for updates

Brittany A. Cymes [1,2] ✉, Katherine D. Burgess [2] & Rhonda M. Stroud [2,3]

The Moon's surface is directly exposed to the space environment and subject to alteration by space weathering. One agent of space weathering, the solar wind, enriches the lunar surface with helium. Although we understand how helium is delivered to the Moon, certain aspects of helium concentration processes on the surface remain unknown, such as why impact-generated glass aggregates contain more helium than equally sized soil grains of other types. Here we have analyzed the contents of vesicular iron nanoparticles in lunar impact glasses using aberration-corrected scanning transmission electron microscopy and electron energy loss spectroscopy and show that the nanoparticles contain high concentrations of helium (10-24 atoms/nm^3). The widespread occurrence of vesicular iron nanoparticles among lunar samples suggests that they may be an important helium reservoir. These results also suggest that space weathering of iron-rich minerals plays a role in helium sequestration on the Moon and potentially on other airless bodies.

Helium-3 is a rare isotope of helium used in advanced technologies like cryogenics, neutron detection, medical imaging, and in the production of electricity by nuclear fusion[1]. In comparison to Earth—where total helium-3 reserves amount to less than 10 kg or 5 parts per trillion—the Moon's surface soil contains a relatively high concentration due to the implantation of this isotope by the solar wind, a stream of charged particles released from the Sun's corona. The average ^{4}He/^{3}He ratio of the solar wind is 2350 ± 120[2]. Conservative estimates of helium-3 concentrations in lunar soil are 3.7 parts per billion in highland areas and 7.8 parts per billion in maria[3]. As global demand for helium-3 continues to rise, the Moon represents a potential reservoir to supply both Earth and the future cislunar economy[1,4]. Characterizing the nature and distribution of helium-3 represents an important milestone toward realizing this future, and such efforts also serve to constrain the Moon's surface evolution over time, including how valuable helium-3 reservoirs develop in the first place by space weathering.

Airless planetary bodies such as the Moon, Mercury, and asteroids experience progressive surface evolution due to space weathering processes, which include solar wind irradiation and micrometeoroid impacts[5]. Because of their complex interactions with the surface, these processes can produce a range of alteration products. For example, impacts progressively pulverize surface material into increasingly smaller particles. At the same time, the energy released from impacts can melt and/or vaporize both target and impactor, coating surrounding grains with mixed material. Solar wind ions —~96% H$^+$ and 4% He^{2+}(see ref. 6)—both sputter surface material and

implant into individual soil grains, causing amorphization and vesiculation. Though the solar wind is responsible for implanting helium into lunar regolith, further impact processing may influence its distribution and concentration. Thus, we cannot evaluate lunar helium reservoirs without considering space-weathering interactions with the surface.

Despite the complex, open-system nature of space weathering, researchers have established some key trends. The concentration of helium in lunar regolith correlates to the surface exposure age of the soil, the solar wind fluence at a particular location, and the amount of titanium and iron in the soil[7–9]. Both titanium and iron are primary components of the mineral ilmenite, the most abundant opaque mineral in lunar rocks[10], which retains helium more effectively than the bulk soil silicate phases[11]. Helium has been measured in situ in lunar material only in the minerals ilmenite and chromite[12], both oxide minerals through which helium diffusion rates are slower than the surrounding silicate minerals[13].

Another unexplained trend is the high concentration of helium in agglutinates—complex aggregates of dark glass-welded fines—relative to equally sized bulk soil grains of other types[14]. In addition, helium concentrations increase as agglutinate particles get smaller, irrespective of iron content, and are concentrated in the sub-100 μm size fraction[14]. In this investigation, we suggest that these trends are due to the presence of vesicular nanophase metallic iron particles (v-npFe^0)[15]. We show that the widespread v-npFe^0 contain high concentrations of helium and discuss how they may represent an important helium reservoir on the surface of the Moon.

[1]Jacobs, NASA Johnson Space Center, Houston, TX, USA. [2]Materials Science and Technology Division, U.S. Naval Research Laboratory, Washington, DC, USA. [3]School of Earth and Space Exploration, Arizona State University, Tempe, AZ, USA. ✉e-mail: brittany.a.cymes@nasa.gov

Results

Vesicular metallic iron nanoparticles in lunar soil

We found v-npFe^0 in grains from each of the seven lunar soil samples investigated, examples of which are shown in Fig. 1. The v-npFe^0 are near-spherical to irregularly rounded in shape and exhibit varying numbers of vesicles of differing shapes and sizes on their surfaces. We identified two general types of v-npFe^0. The first are large v-npFe^0, defined as those >15 nm in diameter, found exclusively within agglutinitic glass particles (Fig. 1a–c) and melt splashes on lunar grain surfaces (Fig. 1d, e). The second are small v-npFe^0, defined as those <15 nm in diameter, which are also found within agglutinitic glass particles (Fig. 1b, c) and melt splashes on mineral and glass grain surfaces (Fig. 1d, e), but also in solar wind-irradiated rims (Fig. 1f, g) and vapor-deposited rims on mineral and glass grains (Fig. 1h, i). In agglutinitic glass and melt splashes, large v-npFe^0 either occur in groups, typically mixed with small npFe^0 and v-npFe^0 (Fig. 1a–e), or as solitary large particles (Fig. 1j). Though typically occurring as discrete particles, we also found instances of large v-npFe^0 coalescing with one another (Fig. 1a).

We examined a ~ 5 μm-diameter glass grain that had abundant v-npFe^0 available for analysis within its volume and within melt splashes adhered to its side (Fig. 2a). This glass grain is one example, additional samples are described in the Supplementary Information. The glass grain contained numerous large npFe^0 particles 20–80 nm in diameter distributed throughout its volume and both large and small v-npFe^0 near the surface. Lattice fringe imaging (Fig. 2b, c and Supplementary Information Fig. S1) and electron energy loss spectroscopy (EELS) spectrum imaging (Fig. 2d, e

and Supplementary Information Fig. S2) indicate that the npFe^0 and v-npFe^0 are metallic α-iron.

We observed a relationship between the depth of npFe^0 from the surface of the grain and whether they were vesiculated. In agglutinitic glass particles ≤100 nm in diameter and in melt splashes ≤50 nm thick, v-npFe^0 are typically found throughout the full volume (Fig. 1b and Supplementary Information Figs. S2g, S3e, and S4a, b). In irradiated and vapor-deposited rims, small v-npFe^0 occur only within $\sim$50 nm of the surface, and those positioned deeper are not vesicular (Fig. 1g, i and Supplementary Information Fig. S5). In melt splashes (Supplementary Information Fig. S4c, d) and large glass grains (Figs. 1c and 2a), v-npFe^0 are found only within $\sim$50–100 nm of the surface. The implantation depth of 4 keV He^{2+} (typical of solar wind) is $\sim$35 nm in bulk silicate according to binary collision models[16] though interstitial helium can diffuse further into grains. The depth-dependent relationship observed suggests that v-npFe^0 are products of He^{2+} implantation.

Identification of helium in vesicular nanophase metallic iron particles

In the glass grains measured, we detected helium within many of the large v-npFe^0 and those we quantified had concentrations ranging from 10 to 24 atoms/nm^3. The round to irregularly shaped vesicles of the particles measured ranged from $\sim$10 to 20 nm in diameter, and the position of the He K-edge peak varied from 22.8 to 24.3 eV (Figs. 1j, 3c, and 4a and Supplementary Information Fig. S6a). In one v-npFe^0 particle in the 79221 glass grain, we measured five different helium concentrations ranging from 15 to
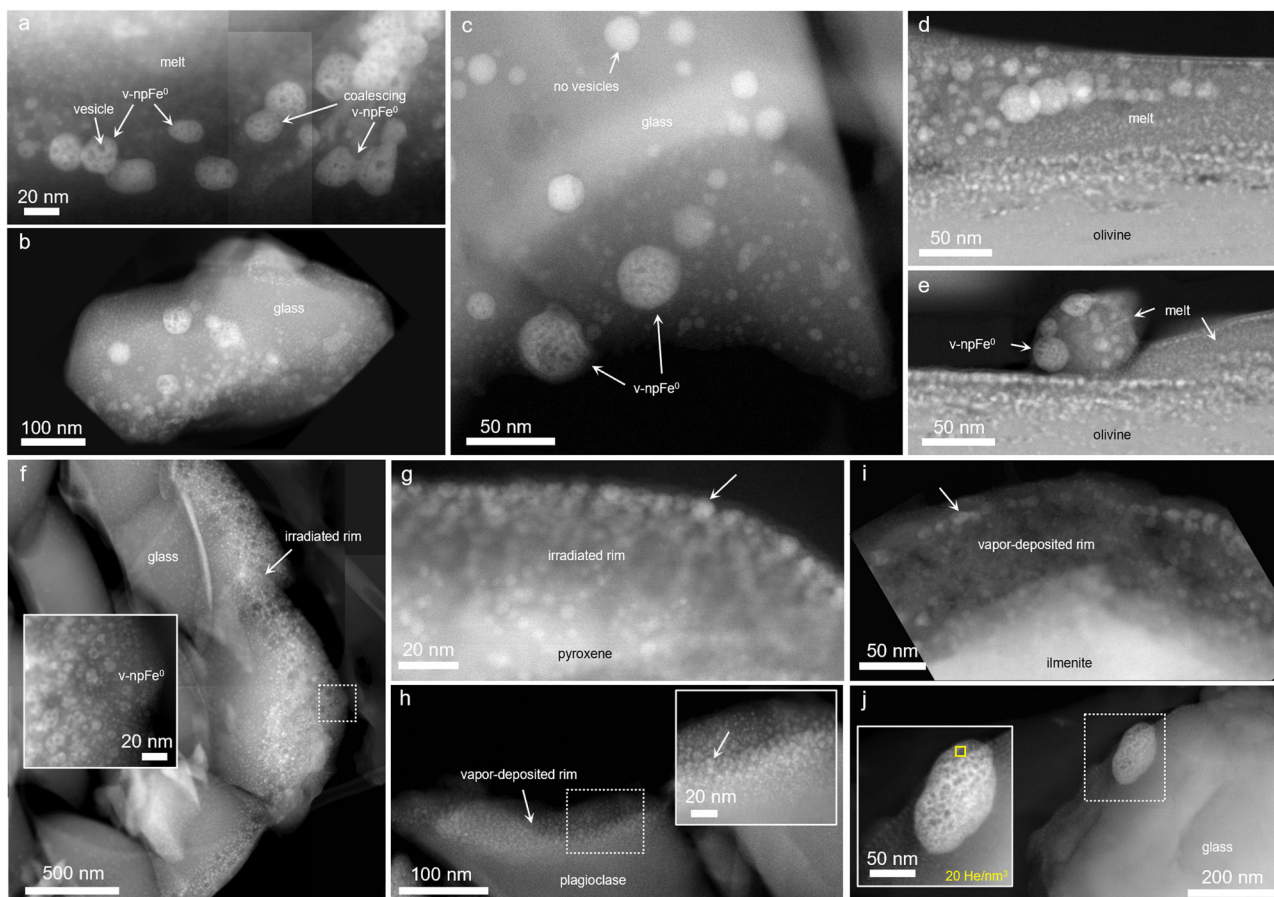

Fig. 1 | High-angle annular dark field images of helium-bearing vesicular metallic iron nanoparticles (v-npFe^0) found in lunar soil grains. a–c Large and small v-npFe^0 within agglutinitic glass grains in lunar soils 76241 (**a**), 76240 (**b**), and 72501 (**c**). **d, e** Large and small v-npFe^0 within a melt splash (**d**) and melt droplet (**e**) on an olivine particle in 76241. **f, g** Small v-npFe^0 within solar wind-irradiated rims of a glass grain in soil 76261 (**f**) and a pyroxene grain in soil 76261 (**g**). **h, i** Small v-npFe^0 within vapor deposited rims of a plagioclase grain in soil 76261 (**h**) and an ilmenite grain in soil 76241 (**i**). **j** A solitary large v-npFe^0 at the surface of a glass grain in soil 76240 with helium concentration shown in yellow.

Fig. 2 | A space-weathered glass grain from lunar soil 79221 containing vesicular nanophase metallic iron particles (v-npFe⁰). a A cross-section of the glass grain showing v-npFe⁰ near the surface and npFe⁰ in interior. **b** Large and small v-npFe⁰ within the area indicated in (**a**). **c** A higher magnification image of the dashed region of (**b**) showing the lattice fringes of the large v-npFe⁰; inset: the Fast Fourier Transform of (**c**) showing a 2.0 Å d-spacing corresponding to (110) of α-Fe. **d** A melt splash region indicated in (**a**) with large and small v-npFe⁰. **e** The EELS spectra in the range 680–750 eV of the dashed region of (**d**) showing the Fe $L_{3,2}$-edge of v-npFe⁰ (solid line) compared to that of a metallic iron standard (dashed line).
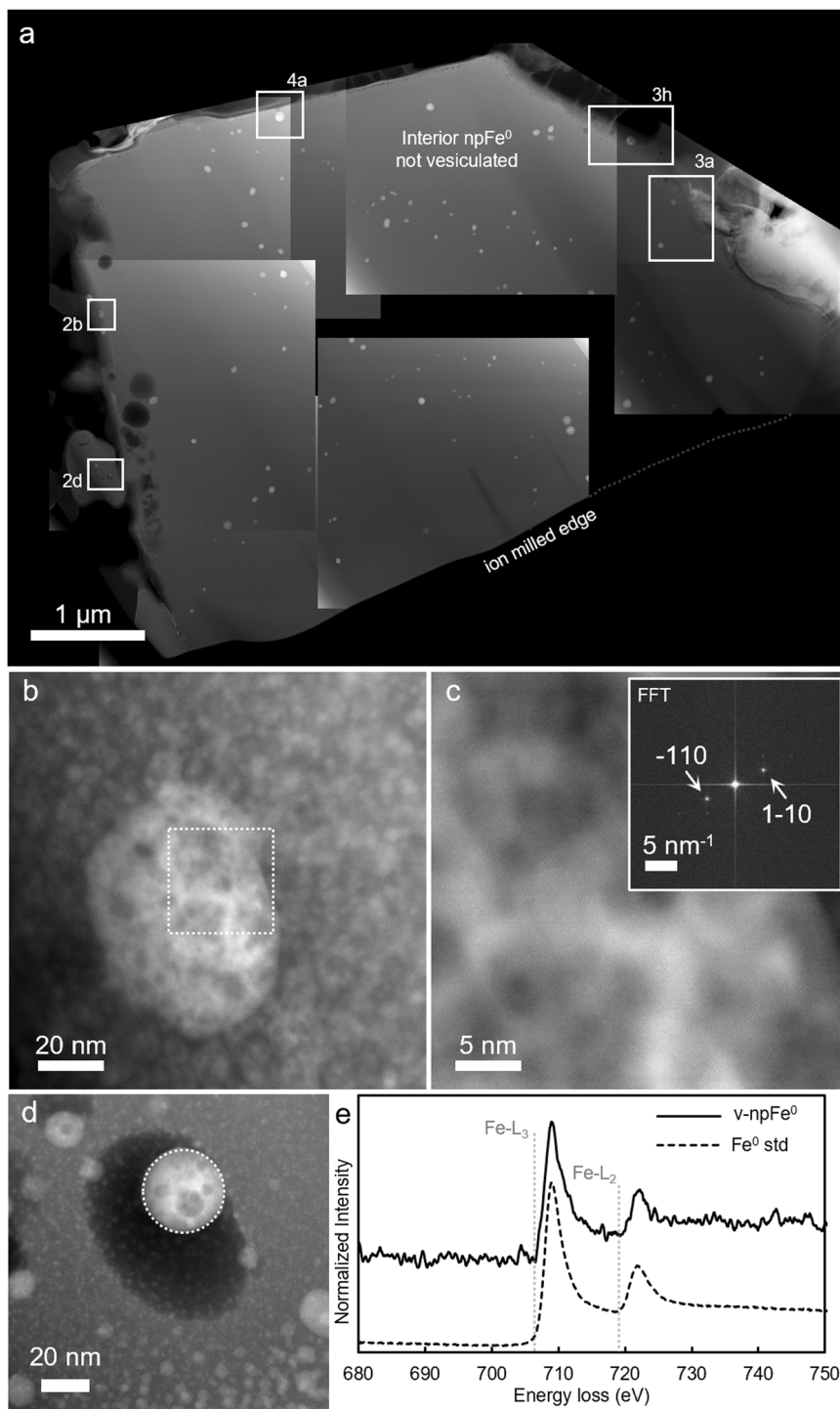
24 atoms/nm³ (Fig. 3c, d). When different helium concentrations are measured within a single v-npFe⁰ particle, we assume multiple vesicles are present, each with their own internal pressure[17]. In contrast, when the helium concentration is the same among multiple vesicles in a v-npFe⁰ particle, the vesicles may be connected[17].

Each of the studied soil samples contained helium-bearing large v-npFe⁰ (Supplementary Information Fig. S2). There is a clear relationship between the vesicles in the images and the He K-edge in the EELS spectra of the vesicles, whereas the He K-edge is absent in the solid portions of the v-npFe⁰ and in the surrounding glass matrix (Fig. 3a, b and Supplementary Information Fig. S2). Multiple linear least squares fitting models of the EELS spectrum images further show a strong spatial correlation between the He

K-edge and the vesicles, demonstrating that helium is concentrated inside the vesicles (Fig. 4 and Supplementary Information Fig. S6).

Despite the disruption of the particle morphology by extensive vesiculation, there is no evidence of strain in the crystal structure of the v-npFe⁰ (Fig. 3c and Supplementary Information Fig. S1). In the samples we analyzed, large v-npFe⁰ were often the only vesicular phase present in the vapor-deposited rims, agglutinate grain surfaces, and melt splashes. But in the cases where v-npFe⁰ were present in a vesicular rim matrix (e.g., Fig. 3), the matrix vesicles did not contain helium, demonstrating that v-npFe⁰ are more retentive of helium relative to other phases.

Although we assume that small v-npFe⁰ contain or contained helium at one point, because their vesicles were typically <1 nm, it was challenging to

Fig. 3 | Electron energy loss spectroscopy of vesicular nanophase metallic iron particles (v-npFe⁰) from lunar soils showing the presence of helium in the vesicles. a The region indicated in Fig. 2a showing a v-npFe⁰ near the grain surface and a npFe⁰ in the grain interior; inset: a v-npFe⁰ particle from region indicated in (**a**) with dashed boxes indicating areas where EELS spectra were summed. **b** The EELS spectra from the glass, particle, and vesicle regions indicated in (**a**, inset). **c** The region indicated in Fig. 2a showing a v-npFe⁰ in a rim containing vesicles and small v-npFe⁰ with helium concentrations for each vesicle shown in yellow; insets: high magnification image and corresponding Fast Fourier Transform of the black-dashed region in (**c**) showing lattice fringes of the v-npFe⁰ and a 2 Å d-spacing corresponding to (110) of α-iron. **d** The EELS spectra from six different regions in (**c**) outlined in white-dashed lines showing ~1 eV variation in helium K-edge position compared to the nanoparticle matrix.
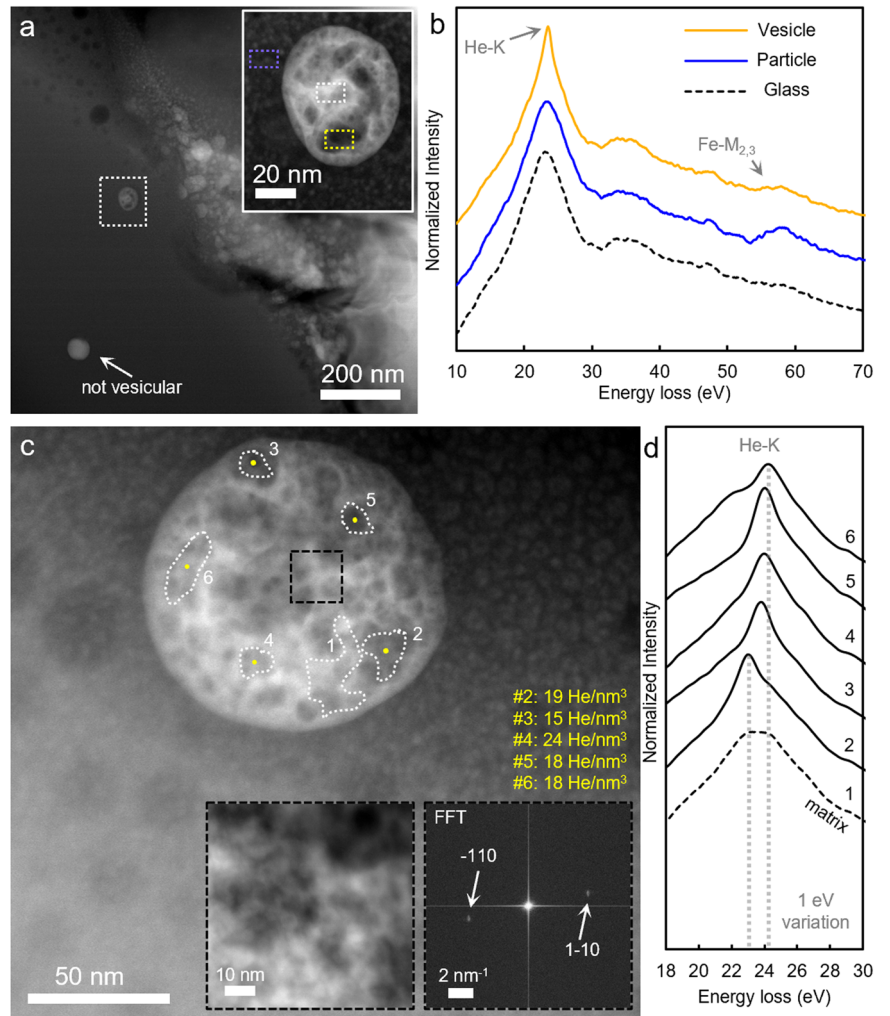
Fig. 4 | A partially vesiculated, helium-bearing nanophase metallic iron particle.
a, b A npFe⁰ situated 85 nm from the surface of a glass grain from soil 79221 with vesicles only on the surface-facing side. **c** The low-loss EELS spectra summed from regions indicated in (**b**) showing the presence of the He K-edge in the vesicle region and the Fe M-edge in the non-vesiculated particle region compared to the glass matrix region. **d** A map of components from the multiple linear least squares fitting of the reference spectra shown in (**c**) showing strong correlation between the He K-edge and the vesicles.

distinguish the He K-edge against the large background contribution of the sample and the poor signal-to-noise ratio also made the measurement difficult. Large v-npFe[0] in some areas lacked helium entirely, despite the analytical conditions being optimal (Fig. 1a).

We also observed npFe[0] with single vesicles in samples 76261 and 79221, resembling oxidized iron core-shell particles described previously[18], but found that these shells were instead comprised of metallic iron rather than iron oxide and their cores contained helium (Supplementary Information Fig. S7). However, we did find a few instances oxidization. For example, helium-bearing v-npFe[0] with surface oxidation were observed on the edge of a glass grain in 72501 (Supplementary Information Fig. S2a–c) and on the surface of a melt splash in 76421 (Supplementary Information Fig. S3e). We also observed a few examples of npFe[0] with oxidized surfaces in samples 76261 and 72501 (Supplementary Information Fig. S3a–c).

Partial vesiculation of a nanophase metallic iron particle

The glass grain from soil 79221 contained a v-npFe[0] that was conspicuous among those we observed as it was only partially vesiculated. The v-npFe[0] was 100 nm in diameter, and its center point was 85 nm from the surface of the glass (Fig. 4a). Only the side facing the surface of the glass was vesiculated, and helium was measured in the vesicles (Fig. 4b, c). The multiple linear least squares fitting of the glass, the iron metal matrix, and the vesicle reference spectra show a clear spatial correlation between the He K-edge and the vesicles (Fig. 4d).

Discussion

Particles morphologically similar to v-npFe[0] have been observed previously in space-weathered lunar material returned by the Apollo program. Oxidized, hollow iron nanoparticles have been described within a glass grain in mature soil 79221[18] and v-npFe[0]-like particles of different sizes have been observed near the surface of a glass grain in mature soil 79221, within an olivine rim in sub-mature soil 71501, and in an amorphous rim on a plagioclase grain in immature soil 71061[15]. The relationship between npFe[0] depth in a grain and whether it is vesiculated has also been documented in Apollo grains[15]. Although these studies of hollow or vesicular npFe[0] in Apollo samples have included EELS analysis, such studies were focused on the core-loss region to determine iron oxidation state, rather than the low-loss region where helium may have been detected[15,18].

In mature lunar samples returned by the Chang'E-5 mission, several ~10 nm v-npFe[0] were observed in silicon-rich material in the space-weathered rims of olivine grains; however, helium was not detected with low-loss EELS analysis of the vesicles[19]. As we observed here, helium is not always present or detectable in v-npFe[0] for several potential reasons, such as natural diffusion, heating, perforation during sample preparation, beam-induced diffusion during spectrum image acquisition, sample thickness, or other measurement parameters, such the energy spread of the beam, and the sensitivity of the EELS detector.

In addition to lunar samples, hollow iron and iron sulfide particles have been identified in GEMS (Glass with Embedded Metal and Sulfides)[20]. GEMS are components of interplanetary dust particles and are considered among the most primitive materials in the Solar System[21,22]. Though the hollow metal particles in GEMS grains have not been studied with EELS to confirm if helium is present, their relation to solar wind irradiation has been considered[20]. In addition, metal particle agglomeration similar to that observed here (Fig. 1a) has been documented in a GEMS grain and identified as a condensation product[20]. Both the present study and prior work demonstrate that v-npFe[0] occur in many space-weathered lunar regolith grains ranging in maturity. Out data also support helium implantation as a possible origin for vesiculated metal observed in GEMS.

Hollow and vesicular npFe[0] have been previously described as potentially representing different stages of the Kirkendall oxidation effect[15,18], a nonequilibrium interdiffusion process at the interface of two metals such that vacancy diffusion inward occurs to compensate for unequal material flow outward[23]; however, our observations indicate that v-npFe[0] do not form by this process. If v-npFe[0] formed by the Kirkendall effect, we should

observe lower-density oxide shells surrounding the particles and the coalescence of voids at the interface, rather than the complex network of differently sized voids[24]. Some oxidized shell textures observed in lunar soil 71061[15] and during our analysis (Supplementary Information Fig. S3) more closely resemble early stages of the Kirkendall effect, where a solid metallic core is surrounded by a hollow shell which is itself surrounded by an oxidized shell[25]. Other indicators that v-npFe[0] are not products of the Kirkendall effect are that (1) v-npFe[0] are metallic iron, (2) the vesicles are filled with helium, and (3) there is a relationship between npFe[0] depth in their host grain and whether they are vesiculated. These lines of evidence, in addition to our observation of a partially formed v-npFe[0] (Fig. 4), suggest that helium ions implant into existing npFe[0] and form v-npFe[0].

The behavior of helium in metals has been widely studied because helium accumulates in nuclear energy systems due to neutron irradiation. In nuclear energy systems, helium atoms are produced within the sample and atomistic models reflect those conditions[26,27]. Complimentary studies have implanted helium in α-iron and other metals to describe bubble development[28,29]; however, the applicability of these studies to v-npFe[0] is limited as they simulate more extreme conditions than those found on the Moon. Further, although studies have focused on implanting helium into materials for the purposes of producing iron nanoparticles[30] and others have performed co-implantation of iron and helium in ferritic alloys to optimize helium sequestration[31], little is known regarding the influence of ion implantation on existing nanoparticles.

In many metal structures, once the concentration of interstitial helium atoms exceeds the planar yield strength, helium precipitates into bubbles[32]. Once these bubbles grow to such a diameter that they encounter free surfaces, they form blisters and rapidly burst[33,34]. It follows that this process might be accelerated in nanoparticles; however, the v-npFe[0] observed here are embedded in glass, so there are no free surfaces, only interfaces, which are known to trap implanted helium[35]. In metal alloys, the crystal structures accommodate strain by confining helium to semicoherent interfaces as nanoscale platelets[36–38] or to interfaces in precipitate-matrix nanostructured alloys[31]. These examples describe crystalline interfaces; however, there are examples of helium bubble stability at crystalline-amorphous interfaces[39], but not in nanoparticle–matrix geometries. The lunar v-npFe[0] observed here represent an example of helium stability at a crystalline-amorphous interface in a nanoparticle-matrix geometry in naturally occurring samples.

The widespread production of npFe[0] as a result of space weathering is widely known to attenuate the characteristic spectral signatures present in remotely sensed optical data[5]. For this reason, how npFe[0] form and the nature of their distribution on the Moon are subjects of great interest. Based on our results showing widespread helium-bearing v-npFe[0] on the Moon, we propose considering that the production of npFe[0] may also play an important role in the lunar helium cycle. Helium is a component of the lunar exosphere and questions remain regarding the contribution of endogenic helium to its budget. It is important to establish how helium is retained in the regolith so that we can better predict its release characteristics, which have been shown to vary[1,40,41]. In this light, the production of v-npFe[0] through progressive space weathering may result in the lunar surface becoming more retentive of helium over time as the soil is further broken down and reworked.

Based on our observations, we propose that the reason helium concentrations are higher in agglutinates than in equally sized bulk soil grains of other types[14] is because agglutinates often contain large npFe[0] which can capture and retain helium. Moreover, the mechanism governing why helium concentrations increase as agglutinate particle sizes decrease—irrespective of iron content—is npFe[0] in smaller agglutinate particles residing at accessible helium implantation depths. In addition, agglutinates typically have irregular shapes and thus greater surface area, allowing for more chances for npFe[0] to be irradiated by helium to produce v-npFe[0].

Although npFe[0] are typically considered to be a final space weathering product, their evolution in response to continual weathering has not yet been fully considered. Our results suggest that the npFe[0] in agglutinates and the npFe[0] in the space-weathered rims of mineral grains can transform into

v-npFe^0 by continual solar wind irradiation. There are several aspects that remain unconstrained, such as whether helium-bearing v-npFe^0 survive multiple impact events or not, though our results showing agglomeration of helium-poor v-npFe^0 suggest the latter. There are also fundamental questions remaining regarding impact energy, melt composition and cooling rate, and how these might influence v-npFe^0 formation that should be considered in future studies. Furthermore, it will be important to characterize how this helium reservoir might be accessed—e.g., by crushing or heating—as well as the environmental impact. Nevertheless, v-npFe^0 are unique secondary alteration products, and may be of great significance with respect to in situ resource utilization because they indicate that progressive metallization of the lunar regolith by space weathering may represent an important precursor to helium enrichment and may also influence lunar helium exospheric cycling.

Methods

Sample selection and preparation
The soil samples analyzed in this study were collected during the Apollo 17 mission. The soils range from submature to mature and include <45 μm size fractions of soils 72320/1 (I_S/FeO = 73.0), 72501 (I_S/FeO = 81.0), 76240/1 (I_S/FeO = 56.0), 76261 (I_S/FeO = 58.0), and 79221 (I_S/FeO = 81.0)[42]. Soil grains were prepared for analysis in the scanning transmission electron microscope (STEM) by ultramicrotome sectioning or by focused ion beam in a scanning electron microscope. For the samples prepared by ultramicrotome, soil grains were embedded in epoxy and sectioned to electron transparency (80–100 nm) using a diamond knife. The sections were supported on 3 mm lacey carbon-coated copper grids. For the samples prepared by focused ion beam, soil grains were first dispersed onto carbon tape adhered to an aluminum pin-stub and coated with ~80 nm of amorphous carbon. Grains with surface textures indicative of space weathering were identified and prepared using an FEI Helios G3 dual beam focused ion beam scanning electron microscope. Each selected grain was first protected with ~100 nm of electron beam-deposited carbon followed by 1-1.5 μm of ion beam-deposited carbon and thinned to ~1 μm using a 30 keV gallium ion beam. After welding the thinned sample to a copper half-grid using platinum, the samples were thinned using progressively lower currents and accelerating voltages until a final thickness of <100 nm was achieved. We prepared 2–3 ultramicrotome grids from each sample and examined ~15–20 grain-clusters on each grid and prepared and examined 1–2 ~ 10 × 10 μm focused ion beam cross sections from each sample.

Scanning transmission electron microscope (STEM) imaging
The STEM analysis was carried out using a C$_S$-corrected Nion UltraSTEM200-X at the U.S. Naval Research Laboratory. Prior to introduction into the ultra-high vacuum STEM, the samples were held under vacuum at ~20 °C for 48 h to drive off adsorbed water. The STEM was operated at 200 keV and 40 pA, with an ~0.1 nm diameter probe. The STEM images were collected using a high-angle annular dark field (HAADF) detector, where contrast is a direct function of atomic number and sample thickness.

Electron energy loss spectroscopy (EELS) measurements
The EELS data were acquired using a Gatan Enfinium ER dual EELS spectrometer on the Nion UltraSTEM200-X. The EELS data were acquired as spectrum images, where a spectrum from a specified energy range is acquired at each pixel in a selected area of the sample. The EELS spectrum image data provide information about sample thickness, elemental composition, and chemical states with spatial context. The EELS spectrum image pixel sizes varied depending upon the size of the region analyzed and 2048 energy channels were collected at a 0.05 eV/channel dispersion. The energy resolution as measured from the full-width half maximum of the zero-loss peak was 0.45 eV. The spectrometer collection semi-angle was 50 mrad and the entrance aperture was 2.0 mm.

The EELS spectrum image data were acquired sequentially in the range −10–90 eV for the zero-loss peak at an exposure of 5×10^{-5} s px^{-1},

12–105 eV for the low-loss region at 1×10^{-3} s px^{-1}, and 660–760 eV for the Fe L-edge (~708 eV) at 1×10^{-2} s px^{-1}. The EELS spectrum image data were processed using DigitalMicrograph software. Scan-related energy drift was corrected for by calculating a peak shift map from the zero-loss peak and applying the shift to the other spectrum images in each acquisition series. Plural scattering was removed using the Fourier-ratio method and X-ray spikes were removed with a 5.0 σ deviation limit. The background was removed from the Fe L$_{3,2}$- edge using a Power-law (AE^{-r}) and the background for the He K-edge was subtracted by another method detailed below.

Mapping and quantification of helium
The He K-edge occurs in the low-loss region at ~22 eV (1 s → 2p transition) where it overlaps with the iron metal bulk plasmon peak. To isolate the He K-edge from the plasmon for signal mapping, a multiple linear least squares fitting routine was used. For this, background-subtracted reference spectra for the bulk matrix phase, the npFe^0, and the vesicles were first identified. A fitting was then performed for each pixel in the spectrum image and fit integral maps for each reference component were generated, as well as maps of residual signal and reduced chi-squared. The multiple linear least squares fitting routine was judged successful when the residual signal map showed no remaining signal or sparse isotropic noise and when the reduced chi-squared map had flat, featureless contrast. The individual fit integral maps were then overlain to produce a multiple-component map.

The energy of the He K-edge can vary by up to ~3 eV corresponding to variations in the density of helium atoms in each vesicle[17]. The concentration of helium trapped in v-npFe^0 vesicles was determined using a method[43] that has been used to determine helium density in bubbles within several materials, including martensitic steel[44], lunar ilmenite[12], and palladium tritides[45]. The background subtraction for the low-loss region was accomplished by normalizing the npFe^0 matrix spectrum to the vesicle spectrum and then subtracting the latter from the former. Where this procedure was insufficient owing to substantial background contributions from npFe^0 or glass, the background was removed in one or two steps using a second-order polynomial function and a linear function. The helium concentration within each vesicle was then calculated from

$$n_{He} = \frac{I_{He}}{\sigma I_{ZLP} d} \qquad (1)$$

where n_{He} is the number of helium atoms/nm^3, I_{He} is the integrated intensity of the helium peak at the center of the vesicle after background removal as described above, σ is the helium cross-section calculated at our microscope parameters, I_{ZLP} is the integrated intensity of the zero-loss peak, and d is the absolute vesicle thickness calculated at the center of the vesicle by Kramers–Kronig analysis. Two different methods for determining σ yield values that vary by ~25%, which contribute to error in the density calculation[43,46]. Another source of error for this method is the calculation of d, which can vary pixel by pixel. Relative errors for this method are available in published analyses which used the same instrument and analytical conditions as were used here[12]. Finally, although multiple EELS spectrum image scans are known to diminish the helium density of bubbles in silicon, such effects can be mitigated by reducing the pixel dwell time[47]. We acquired the zero-loss spectrum image at a very short pixel dwell time before the low-loss spectrum images were acquired and thus, we do not expect loss of helium. Multiple scans at low-loss dwell times confirm this, though dwelling a stationary beam on a vesicle has been observed to perforate and evacuate the vesicle contents[12].

Data availability

References

1. Kuhlman, K. R. & Kulcinski, G. L. Helium isotopes in the lunar regolith—measuring helium isotope diffusivity in lunar analogs. In *Moon: Prospective Energy and Material Resources* 23–56 (ed Badescu, V.) (Springer Berlin Heidelberg, 2012).
2. Geiss, J., Bühler, F., Cerutti, H., Eberhardt, P., Filleux, C. Apollo 16 Preliminary Science Report, *NASA SP-315*, p. 14–1 (1972).
3. Taylor, L. A. & Kulcinski, G. L. Helium-3 on the moon for fusion energy: the Persian Gulf of the 21st century. *Solar Syst. Res.* **33**, 338 (1999).
4. Borowski, S. K. & Sauls, B. G. The commercial passenger transport: precursor to routine travel between the Earth and the Moon. *ASCEND* https://doi.org/10.2514/6.2022-4311 (2022).
5. Pieters, C. M. & Noble, S. K. Space weathering on airless bodies. *J. Geophys. Res. Planet.* **121**, 1865–1884 (2016).
6. Ogilvie, K. W. & Wilkerson, T. D. Helium abundance in the solar wind. *Solar Phys.* **8**, 435–449 (1969).
7. Morris, R. V. Surface exposure indices of lunar soils: a comparative FMR study. In *Proc. Lunar Sci. Conf. 7th*, 315–335 (New York, Pergamon Press, Inc., 1976).
8. Taylor, L. A. Hydrogen, helium, and other solar-wind components in lunar soil—abundances and predictions. In *Engineering, Construction, and Operations in Space II: Proceedings of Space 90, the Second International Conference, Albuquerque, NM,* Apr. 22–26, Vol. 1, 68–77 (American Society of Civil Engineers, 1990).
9. Johnson, J. R., Swindle, T. D. & Lucey, P. G. Estimated solar wind-implanted helium-3 distribution on the Moon. *Geophys. Res. Lett.* **26**, 385–388 (1999).
10. Taylor, L. A. Resources for a lunar base: rocks, minerals, and soil of the Moon. In *The Second Conference on Lunar Bases and Space Activities of the 21st Century*, Vol. 2 (NASA Johnson Space Center, 1992).
11. Signer, P. et al. Helium, neon, and argon records of lunar soil evolution. *Proc. Lunar. Sci. Conf.* **3**, 3657–3683 (1977).
12. Burgess, K. D. & Stroud, R. M. Phase-dependent space weathering effects and spectroscopic identification of retained helium in a lunar soil grain. *Geochimica et Cosmochimica Acta* **224**, 64–79 (2018a).
13. Baxter, E. F. Diffusion of noble gases in minerals, in diffusion in minerals and melts. In *Reviews in Mineralogy & Geochemistry* (eds Zhang, Y. & Cherniak, D. J.) Vol. 72, 509–558 (Mineralogical Society of America & Geochemical Society, 2010).
14. Schultz, L. et al. Noble gas and element distribution in agglutinate grain size separates of different density. *Proc. Lunar Planet. Sci. Conf. 9th* **2**, 2221–2232 (1978).
15. Burgess, K. D. & Stroud, R. M. Coordinated nanoscale compositional and oxidation state measurements of lunar space-weathered material. *J. Geophys. Res.: Planets* **123**, 2022–2037 (2018b).
16. Ziegler, J. F., Ziegler, M. D. & Biersack, J. P. SRIM—the stopping range of ions in matter 2010. *Nucl. Instruments Methods Phys. Res. Sec. B: Beam Interact. Mater. Atoms* **268**, 1818–1823 (2010).
17. Jäger, W. et al. Density and pressure of helium in small bubbles in metals. *J. Nucl. Mater.* **111**, 674–680 (1982).
18. Thompson, M. S., Zega, T. J., Becerra, P., Keane, J. T. & Byrne, S. The oxidation state of nanophase Fe particles in lunar soil: Implications for space weathering. *Meteoritics Planetary Sci.* **51**, 1082–1095 (2016).
19. Guo, Z. et al. Nanophase iron particles derived from fayalitic olivine decomposition in Chang'E-5 lunar soil: implications for thermal effects during impacts. *Geophys. Res. Lett.* **49**, e2021GL097323 (2022).
20. Matsuno, J., Tsuchiyama, A., Miyake, A., Nakamura-Messenger, K. & Messenger, S. Three-dimensional observation of GEMS grains: their high-temperature condensation origin. *Geochim. Cosmochim. Acta* **320**, 207–222 (2022).
21. Bradley, J. P. & Dai, Z. R. Mechanism of formation of glass with embedded metal and sulfides. *Astrophys. J.* **617**, 650–655 (2004).
22. Keller, L. P. & Messenger, S. On the origin of GEMS grains. *Geochimica et Cosmochimica Acta* **75**, 5336–5365 (2011).
23. Yin, Y. et al. Formation of hollow nanocrystals through the nanoscale Kirkendall effect. *Science* **304**, 711–714 (2004).
24. Cabot, A. et al. Vacancy coalescence during oxidation of iron nanoparticles. *J. Am. Chem. Soc.* **129**, 10358–10360 (2007).
25. Wang, W., Dahl, M. & Yin, Y. Hollow nanocrystals through the nanoscale Kirkendall effect. *Chem. Mater.* **25**, 1179–1189 (2013).
26. Borodin, V. A. & Vladimirov, P. V. Diffusion coefficients and thermal stability of small helium-vacancy clusters in iron. *J. Nucl. Mater.* **362**, 161–166 (2007).
27. Stewart, D., Osetskiy, Y. & Stoller, R. Atomistic studies of formation and diffusion of helium clusters and bubbles in BCC iron. *J. Nucl. Mater.* **417**, 1110–1114 (2011).
28. Brimbal, D., Décamps, B., Barbu, A., Meslin, E. & Henry, J. Dual-beam irradiation of α-iron: Heterogeneous bubble formation on dislocation loops. *J. Nucl. Mater.* **418**, 313–315 (2011).
29. Sabelová, V. et al. Characterization of helium implanted Fe-Cr alloys by means of positron annihilation methods. *J. Nucl. Mater.* **450**, 54–58 (2014).
30. Loeffler, M. J., Dukes, C. A. & Baragiola, R. A. Irradiation of olivine by 4 keV He$^+$: simulation of space weathering by the solar wind. *J. Geophys. Res.* **114**, E03003 (2009).
31. Parish, C. M. et al. Helium sequestration at nanoparticle-matrix interfaces in helium + heavy ion irradiated nanostructured ferritic alloys. *J. Nucl. Mater.* **483**, 21–34 (2017).
32. Trinkaus, H. & Singh, B. N. Helium accumulation in metals during irradiation—where do we stand? *J. Nucl. Mater.* **323**, 229–242 (2003).
33. Wolfer, W. G. The role of gas pressure and lateral stress on blistering. *J. Nucl. Mater.* **93-94**, 713–720 (1980).
34. Galindo, R. E. et al. Protrusion formation and surface porosity development on thermally annealed helium implanted copper. *Nucl. Instruments Methods Phys. Res. Sec. B: Beam Interact. Mater. Atoms* **217**, 262–275 (2004).
35. Demkowicz, M. J., Misra, A. & Caro, A. The role of interface structure in controlling high helium concentrations. *Curr. Opin. Solid State Mater. Sci.* **16**, 101–108 (2012).
36. Chen, D. et al. Self-organization of helium precipitates into elongated channels within metal nanolayers. *Sci. Adv.* **3**, eaao2710 (2017).
37. Beyerlein, I. J. et al. Radiation damage tolerant nanomaterials. *Mater. Today* **16**, 443–449 (2013).
38. Kashinath, A., Misra, A. & Demkowicz, M. J. Stable storage of helium in nanoscale platelets and semicoherent interfaces. *Phys. Rev. Lett.* **110**, 086101 (2013).
39. Jiang, M. et al. Helium bubbles in $Gd_2Ti_2O_7$ borosilicate glass-ceramic composites. *J. Nucl. Mater.* **581**, 154424 (2023).
40. Hodges, R. R. Jr. & Hoffman, J. H. Measurements of solar wind helium in the lunar exosphere. *Geophys. Res. Lett.* **1**, 69–71 (1974).
41. Cook, J. C. & Stern, S. A. Sporadic increases in lunar atmospheric helium detected by LAMP. *Icarus* **236**, 48–55 (2014).
42. Morris, R. V. The surface exposure (maturity) of lunar soils: Some concepts and I_S/FeO compilation. *Proc. Lunar Planet. Sci. Conf.* **9**, 2287–2297 (1978).
43. Walsh, C. A., Yuan, J. & Brown, L. M. A procedure for measuring the helium density and pressure in nanometre-sized bubbles in irradiated materials using electron-energy-loss spectroscopy. *Philos. Mag. A* **80**, 1507–1543 (2000).
44. Fréchard, S. et al. Study by EELS of helium bubbles in a martensitic steel. *J. Nucl. Mater.* **393**, 102–107 (2009).
45. Evin, B. et al. Investigation by STEM-EELS of helium density in nanobubbles formed in aged palladium tritides. *J. Alloys Compounds* **878**, 160267 (2021).
46. Egerton, R. F. *Electron Energy-Loss Spectroscopy in the Electron Microscope*, third edn. (Springer, 2011).
47. David, M.-L. et al. In situ-controlled modification of the helium density in single helium-filled nanobubbles. *J. Appl. Phys.* **115**, 123508 (2014).

Author contributions
B.A.C.: project data curation, formal analysis, investigation, project administration, validation, visualization, writing—original draft; K.D.B.: project conceptualization, data curation, formal analysis, funding acquisition, investigation, methodology, project administration, resources, supervision, validation, writing—review and editing; and R.M.S.: funding acquisition, methodology, resources, supervision, and writing—review and editing.

Competing interests
The authors declare no competing interests.

Additional information
Supplementary information The online version contains supplementary material available at https://doi.org/10.1038/s43247-024-01349-z.

Correspondence and requests for materials should be addressed to Brittany A. Cymes.

Peer review information *Communications Earth & Environment* thanks David Trang and the other, anonymous, reviewer(s) for their contribution to the peer review of this work. Primary Handling Editors: Claire Nichols and Joe Aslin. A peer review file is available.

Reprints and permissions information is available at http://www.nature.com/reprints

Publisher's note Springer Nature remains neutral with regard to jurisdictional claims in published maps and institutional affiliations.